

Journal of Materials Chemistry A

Accepted Manuscript



This is an *Accepted Manuscript*, which has been through the Royal Society of Chemistry peer review process and has been accepted for publication.

Accepted Manuscripts are published online shortly after acceptance, before technical editing, formatting and proof reading. Using this free service, authors can make their results available to the community, in citable form, before we publish the edited article. We will replace this *Accepted Manuscript* with the edited and formatted *Advance Article* as soon as it is available.

You can find more information about *Accepted Manuscripts* in the [Information for Authors](#).

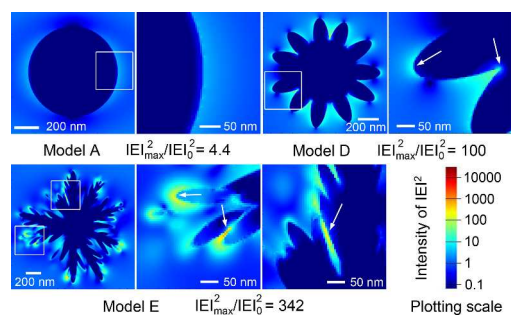
Please note that technical editing may introduce minor changes to the text and/or graphics, which may alter content. The journal's standard [Terms & Conditions](#) and the [Ethical guidelines](#) still apply. In no event shall the Royal Society of Chemistry be held responsible for any errors or omissions in this *Accepted Manuscript* or any consequences arising from the use of any information it contains.

Table of Content Entry

Hierarchical Silver Mesoparticles with Tunable Surface Topographies for Highly Sensitive Surface-enhanced Raman Spectroscopy

Lin cheng, Chuansheng Ma, Guang Yang, Hongjun You and Jixiang Fang**

Surface topographies of hierarchical silver mesoparticles can be well controlled and tuned in a simple aqueous synthesis system. Using FDTD simulation method, the mechanism of the effect of the topographies on the SERS properties is systematically studied.



ARTICLE

Hierarchical Silver Mesoparticles with Tunable Surface Topographies for Highly Sensitive Surface-enhanced Raman Spectroscopy

Cite this: DOI: 10.1039/x0xx00000x

Lin cheng,^a Chuansheng Ma,^b Guang Yang,^b Hongjun You*^a and Jixiang Fang*^a

Using a simple aqueous synthesis method, Ag hierarchical mesoparticles with tunable surface topography are obtained. In this particle-mediated anisotropic growth system, the mechanism of tuning the topographies of the hierarchical mesoparticles is studied. A serial of Ag mesoparticles with well-tuned surface topographies are synthesized as an ideal research target for a systematic investigation of the effect of surface nanostructures on the surface enhanced Raman spectroscopy (SERS) performance. The highly-branched Ag mesoparticles show the highest SERS sensitivity both as single-particle SERS substrate and particle-array SERS substrate, which has an enhancement factor (EF) greater than 10^9 . Using finite difference time domain (FDTD) method, the distribution of localized electromagnetic field near the particle surface is simulated. Based on the simulation result, the mechanism of the effect of topography on the SERS properties is systematically studied.

Received 00th January 2012,
Accepted 00th January 2012

DOI: 10.1039/x0xx00000x

www.rsc.org/

Introduction

Surface-enhanced Raman scattering (SERS) is about amplifying Raman signals by several orders of magnitude, which is mainly attributed to collective oscillations of the conduction electrons through the electromagnetic interaction of light with metals, called surface plasmon resonances (SPR).¹⁻³ Recently, SERS as a powerful analytical tool has a wide potential application in biochemistry, chemical production, food safety and environmental monitoring.⁴⁻⁸ The sensitivity of SERS highly depends on the surface topography of the substrate.⁹⁻¹⁰ The interstitial sites, nanoscaled cavities, and bifurcations constructed on the SERS substrate can produce plasmonic coupling effect which can lead to local surface plasmon resonance (LSPR). The LSPR makes great contribution to the enhancement of SERS.¹¹⁻¹²

Up to now, various kinds of SERS substrates have been synthesized. In general, the SERS substrate, possessing a rough surface, can be classified into three main classes: metallic electrodes, periodic nanostructures, and metallic nanostructured particles.¹² The metallic electrode substrates are prepared through electrochemical deposition, which was initially used to explore SERS discipline and has a great effect on the development of SERS.¹³⁻¹⁴ However, because of the relatively low enhancement factors (EFs) and reproducibility, it has been replaced by periodic nanostructures so as to approach the practical applications. The periodic nanoconstructed substrate is realized by using advanced “top-down” nanopatterning techniques, such as electron beam lithography,¹⁵ nanoimprinting,¹⁶ molecular beam epitaxy,¹⁷ and template-based methods using polystyrene spheres.¹⁸ Using these techniques, it is convenient to

attain regular, uniform and periodic two-dimensional patterns.¹⁹⁻²¹ Nevertheless, it is still difficult to achieve complex three-dimensional nanoscale structure with the current “top-down” technical level. Recently, the metallic nanostructured particles have attracted great interests as SERS substrates due to the fact that fine nanoscale structures can be constructed on the particle surface using “bottom-up” chemical synthesis method. For example, narrow nanogaps down to size of 1 nm were formed on Au and Ag particles, which had EF greater than 10^8 for single-particle SERS.²²⁻²³ These metallic particles with nanotextured surface topographies not only can be used as single-particle SERS substrates but also can be aggregated to form particle-array SERS substrates.²⁴ As single-particle SERS substrate, these particles can be dispersed in solution or delivered into cells through blood flow to detect the Raman signals of molecules located in solutions or cells.²⁵⁻²⁷ As particle-array SERS substrate, the interparticle interactions in the array can produce additional and/or more abundant “hot spots” for SERS.²⁸⁻²⁹

Up to now, some Ag or Au particles with various nanotextured surface topographies have been synthesized and studied as SERS substrates, such as meatball-like,⁹ star-like,³⁰ sea urchin-like,¹² flower-like,³¹ and highly-branched mesoparticles.³² The nanostructured protrusions on these hierarchical particles serving as nano-lightning rods, dramatically increase the electromagnetic field in the vicinity of the tips, and thus generate plenty of enhanced SERS “hot spots” on the surface of particles.³³⁻³⁵ The surface topographies have the important effect on the optical and SERS properties. Although these hierarchical mesoparticles with various nanotextured topographies have been separately synthesized and

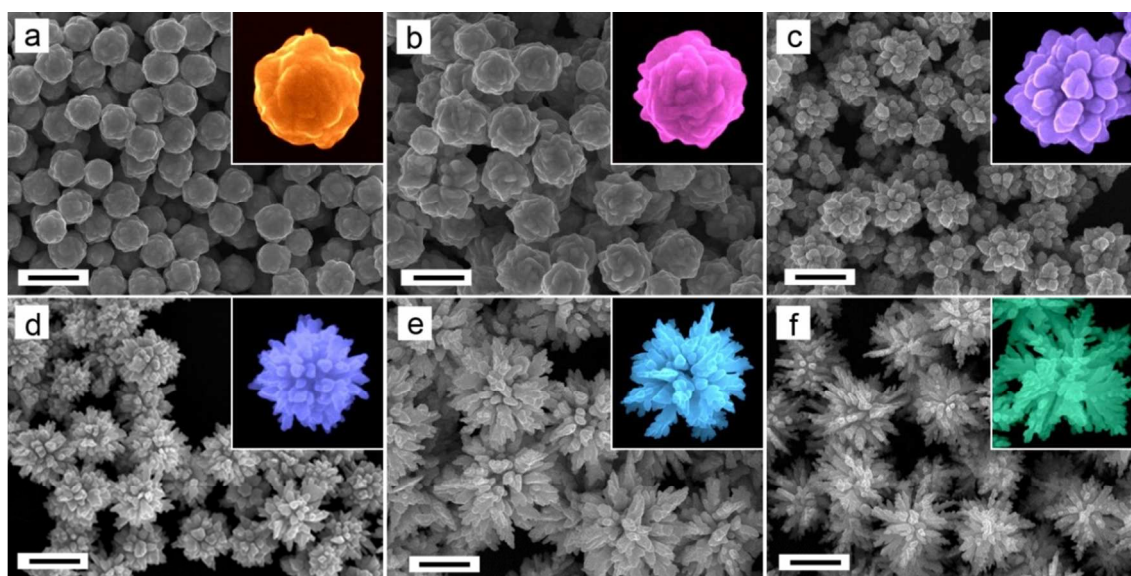


Fig. 1 SEM images of Ag mesoparticles with tunable surface topographies produced by changing the synthesis parameters. The concentrations of AgNO_3 are 1 mM for sample (a) S1, (b) S2, and (e) S5, and 0.5 mM for sample (c) S3, (d) S4, and (f) S6. The concentrations of L-AA are 0.5 mM for S1, 10 mM for S2, S3, and S4, 20 mM for S5, and 50 mM for S6. The reaction times are 20 min for S1, S2, and S5, 15 min for S3, and 10 min for S4 and S6. The rotating rates of magnetic bar are 130 rpm for S1, S2, S4 and S5, 150 rpm for S3, and 200 rpm for S6. The scale bars are 1 μm .

studied as SERS substrates, the systematic investigation for the effect of topographies on the SERS properties is still rather limited. In this paper, a serial of Ag mesoparticles with well controlled surface morphologies are obtained in a very simple synthesis system. Using both experimental measurement and theoretical calculation, the mechanism of topography effect on SERS activities is systematically studied.

Experimental Section

Materials. Silver nitrate (AgNO_3 , 99%) and L-ascorbic acid (L-AA, 99%) were purchased from Sigma Aldrich. Deionized water (Millipore) with resistance of 18.2 $\text{M}\Omega$ was used. The L-AA solutions used in all experiment were freshly prepared.

Synthesis of Ag mesoparticles. In a typical synthesis, 0.05 mL of 100 mM AgNO_3 aqueous solution and 7.45 mL water were mixed in a glass vial. Then 2.5 mL of 200 mM L-AA aqueous solution was added immediately. The reaction was conducted at room temperature with a 200 rpm rotating magnetic bar (the length of the magnetic bar was 3 cm). The colour of the reaction changed from colourless to light grey. After 10 min, the as-synthesized product was centrifuged at 4500 rpm (the length of the rotor was 10 cm, so the linear rate of the rotation was 47 m/s) for 2 min and then washed several times with alcohol and water for further characterization. In the all experimental synthesis of silver particles the total volume of the reaction was fixed at 10 mL and the experimental conditions (reagents concentration, reaction time, and stirring rate) were changed.

Characterization. The morphology of the samples was characterized using field-emission scanning electron microscopy (SEM) (JEOL JSM-7000F) at an accelerating voltage of 20 kV and transmission electron microscopy (TEM) (JEOL JEM-2100) at an accelerating voltage of 200 kV. The Raman spectrum measurements

were carried out on a confocal microprobe Raman spectrometer (LabRAM HR800, HORIBA JOBIN YVON) with 633 nm He-Ne laser line at room temperature. The signal collection time was 1 s for the detection of particles aggregation and 20 s for the single-particle detection with a laser spot of 850 nm diameter. The sample for SERS measurement was prepared through dropping some silver particles dispersion on a clean silicon wafer (7 mm \times 7 mm). After drying, 100 μL of 1×10^{-7} M aqueous crystal violet (CV) solution was dropped on it (keep lucifugal during drying).

FDTD simulation. Based on the SERS samples in Fig. 7, five models were built and their geometric structures were made an approximate treatment. The details of the five models are described in the supporting information. The three-dimensional finite difference time domain (FDTD) simulation was used to calculate electric field distribution and electromagnetic enhancement under the excitation light with wavelengths of 514 nm, 633 nm and 785 nm. The incident light was plane waves which propagated along the z-axis backward and polarized along the x-axis. It was assumed that each geometrical model was suspended in air ($n_0=1.0$). The frequency (ω) dispersive and complex dielectric function for Ag, $\epsilon_{\text{Ag}}(\omega)$, was obtained from the handbook of optical materials. The grid size was 4 nm for the space deviation.

Results and Discussion

Topography Tuning of Hierarchical Silver Mesoparticles

In a simple aqueous solution synthesis system, containing only two reagents, AgNO_3 and L-AA, a serial of hierarchical Ag mesoparticles were obtained. By changing the experimental conditions, such as concentrations of AgNO_3 and L-AA, rotation rate, and reaction times, the topography of silver mesoparticles could be well controlled and tuned. As shown in Figure 1, topographies of the obtained Ag mesoparticles were successfully tuned from meatball-

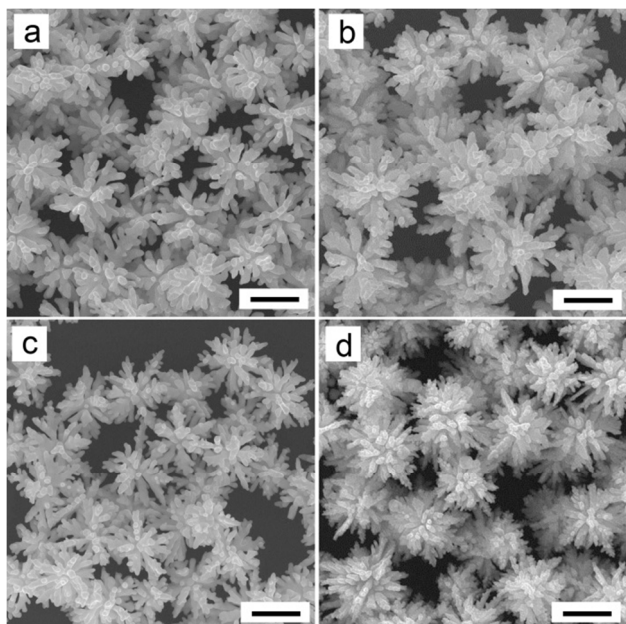


Fig. 2 SEM image of the products obtained with (a) 0.25 mM AgNO_3 and 0.5 mM L-AA, (b) 0.5 mM AgNO_3 and 1 mM L-AA, (c) 0.25 mM AgNO_3 and 10 mM L-AA, (d) 0.5 mM AgNO_3 and 50 mM L-AA. The reaction times all are 20 min. The scale bars are 1 μm .

like shape (Fig. 1a and b) to coral-like (Fig. 1c and d), urchin-like (Fig. 1e), and highly-branched shape (Fig. 1f). All kinds of the hierarchical Ag mesoparticles are found to be uniform in morphology and size. The meatball-like mesoparticles are around 720 nm and 950 nm in diameter, separately in sample S1 and S2, and constructed by the aggregation of nanoparticle units which size is small in S1 and large in S2. From S3 to S5, the bulges on the surface become dense accompanied with the sizes increase in length and decrease in diameter. The particle sizes of S3 to S5 change from about 1 to 2 μm . For the S6, the density of branch reaches maximum and the second sub-branches overgrow on the main branches. The size of the total particle increased to about 1.6 μm .

The synthesis conditions for these Ag mesoparticles are listed in Supporting Information (Table S1). Compared with the reaction time and rotating rate of magnetic bar, the concentrations of AgNO_3 and L-AA have more important effect on the morphology. Keeping the concentration of AgNO_3 at 1 mM, when the concentration of L-AA was changed from 0.5 to 10 and 20 mM, the morphologies of Ag mesoparticles changed from meatball-like shape (sample S1 and S2) to urchin-like shape (sample S5). Keeping the concentration of L-AA at 10 mM, when the concentration of AgNO_3 was decreased from 1 mM (sample S2) to 0.5 mM (sample S4), the bulge on the particle surface becomes longer and thinner. Therefore, both of the increase of L-AA concentration and the decrease of AgNO_3 concentration could improve the protuberated growth.³⁶ If the concentration of AgNO_3 decreased to 0.5 mM and the concentration of L-AA increased to 50 mM, the greatly protuberated anisotropic growth induced a highly-branched morphology (sample S6). From the comparison of sample S3 and S4, the reaction time and rotating rate of magnetic bar also were found having effect on the morphology.

The morphology of the Ag mesoparticles was tuned not only in a wide scope, such as from meatball-like to highly-branched shapes,

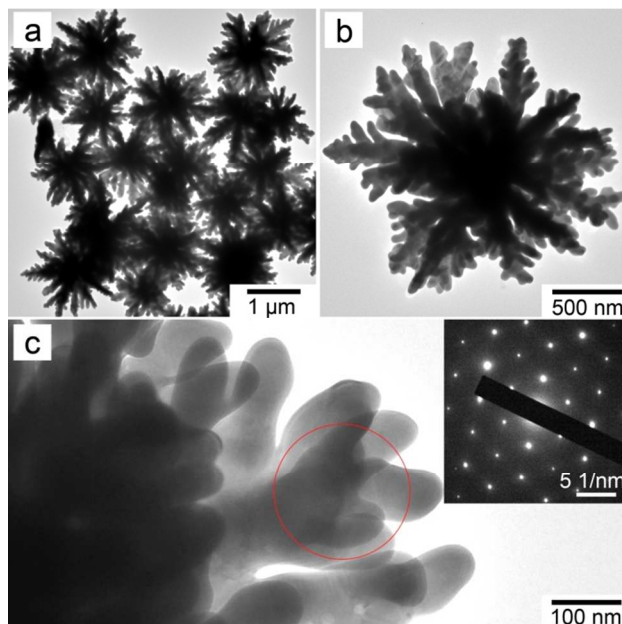


Fig. 3 TEM images of the highly-branched Ag mesoparticles. (a) TEM image of large area of Ag mesoparticles. (b) TEM image of a single typical Ag mesoparticle. (c) High-magnification TEM image of the branches of the coral-like Ag mesoparticle. The inset in (c) shows the correlated SAED patterns from the circled area.

but also could be continuously fine-tuned. As shown in Fig. 2, by slightly changing the concentration of AgNO_3 and L-AA, a serial of coral-like Ag mesoparticles were obtained. At conditions of 0.25 mM AgNO_3 and 0.5 mM L-AA, a coral-like structure with relatively few main and subordinate branches was produced (Fig. 2a). Keeping the concentration ratio constant and changing their concentrations to 0.5 mM and 1 mM, the achieved Ag coral-like structure had more main branches and subordinate branches (Fig. 2b). If we used 0.25 mM AgNO_3 and 10 mM L-AA, the main branches of Ag structure became longer but not abundant (Fig. 2c). Through aborative study, it was found that 0.5 mM AgNO_3 and 50 mM L-AA could produce highly-branched coral-like Ag mesostructures which had more abundant main and subordinate branches (Fig. 2d).

The typical TEM images of highly-branched coral-like Ag mesoparticle synthesized with 0.5 mM AgNO_3 and 50 mM L-AA are shown in Fig. 3. As illustrated in Fig. 3a, the TEM characterization also shows that the particles are uniform in morphology and size. Fig. 3b reveals that the highly-branched Ag particle is composed by many main and subordinate branches. On each main branch, there are several subordinate branches. The length of the main branches ranges from about 450 to 760 nm and the diameter is about 100 nm. For the subordinate branches, the length ranges from 30 to 200 nm and the diameter ranges from 30 to 80 nm. Fig. 3c shows a higher magnification image which indicates the branches being closely grown on the particle surface. The average space between two branches is less than 20 nm. The SAED (selected-area electron diffraction) pattern in the inset of Fig. 3c obtained from branches indicates the branch is single crystal. The composition analysis (Fig. S1) by energy dispersive x-ray spectroscopy shows that except for Si element resulting from the Si substrate, the composition of the red circle area in Fig. S1a is only silver.

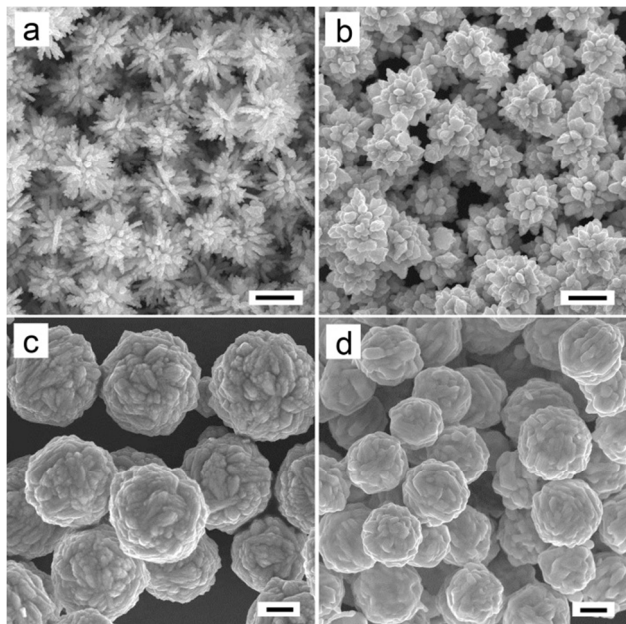
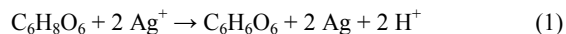


Fig. 4 SEM images of silver mesoparticles synthesized with 50 mM L-AA and different AgNO_3 concentrations: (a) 0.5 mM, (b) 1 mM, (c) 10 mM, and (d) 50 mM. The scale bars are 1 μm .

Mechanism of Topography Tuning

As we found in Fig. 1 and Table S1 that in all of the experimental conditions, the concentrations of AgNO_3 and L-AA have more important effect on the morphology of Ag mesoparticles. The surface topography of the hierarchical Ag mesoparticle can be well tuned by changing the concentrations of AgNO_3 and L-AA. The topography tuning mechanism is studied and discussed, here. Fig. 4 shows the morphology of Ag particles can be tuned in a large range by only changing the concentration of AgNO_3 when all of other conditions keep no change. At the condition of 50 mM L-AA, with the increase of AgNO_3 concentrations from 0.5 to 1, to 10 and to 50 mM, the morphology transforms from highly-branched hierarchical mesoparticle (Fig. 4a) to coral-like mesoparticle (Fig. 4b), and to meatball-like mesoparticle (Fig. 4c and d). The comparison of Fig. 4c and d shows that the size and surface roughness of the meatball-like particles can also be tuned to increase by changing the concentration of AgNO_3 from 50 to 10 mM.

The topography tuning mechanism of the hierarchical mesoparticle through changing concentrations is illustrated in the Fig. 5, using AgNO_3 concentration as example. Xia group has reported the shape transform of Ag coral-like particles at different reaction times using SEM characterization.³² The formation process of the hierarchical Ag mesoparticle is similar with that of the hierarchical Au mesoparticles reported in previous study.^{29,31,37} As shown in Fig. 5a, the formation process is a typical particle-mediated growth mode which can be divided into four stages.³⁸ At first stage, the Ag^+ ions are reduced into Ag atoms by L-AA as following equation described:³⁹⁻⁴⁰



With the reaction proceeding, the concentration of Ag atoms in the solution gradually increases. The change of Ag atoms concentration

is schematically described using the LaMer curve in Fig. 5a. When the concentration of Ag atoms exceeds the supersaturation point of nucleation, the atoms will aggregate to form stable nucleus in the second stage. Thus, a great number of Ag nanoparticles are formed in the solution. At the same time, the concentration of Ag atom dramatically decreases accompanied with the increase of Ag nanoparticle concentration in the solution. When the concentration of Ag atom decreases to below supersaturation point of nucleation, the nanoparticles will stop being produced. In this system, L-AA not only plays as reducing agent, but also acts as capping agents, which adsorbs on the particle surface for the stabilization of the nanoparticles. One L-AA molecule has four hydroxyl groups, so similar with dopa molecule, the L-AA molecules will promote Ag nanoparticles to aggregate through their “glue” function.^{29,31} In the third stage, the Ag nanoparticles aggregate to form spherical mesoparticle through a new and non-classical crystal growth, which is called “particle-mediated growth”.^{38,41} Through particle mediated growth, a polycrystalline or mesocrystal structure can be formed depending on the growth conditions.⁴²⁻⁴³ The particle size of Ag mesoparticles can be described as following equation:

$$r = kT\rho^{2/3}/3\pi\eta f_m \quad (2)$$

where, r is the radius of the mesoparticle, k is the Boltzmann constant, ρ and f_m are the density and suspending aggregation frequency of the nanoparticles, T and η are the temperature and viscosity of the solution. In this synthesis system, the solution is rotated with magnetic bar, so T , ρ , and η are uniform in the whole solution, resulting in uniform distribution of mesoparticle size. In the fourth stage, the remaining Ag ions will be reduced and deposited on

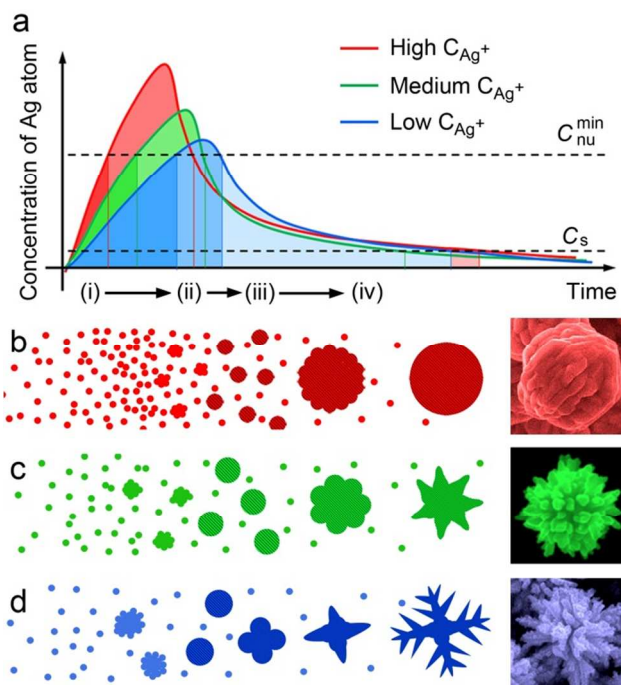


Fig. 5 Schematic illustration of the effect of Ag^+ concentration on the Ag mesoparticle morphology. (a) The effect of Ag^+ concentration on the plot transformation of Lamer curves for the Ag mesoparticle formation. (b-d) The formation process of various Ag mesoparticles with different Ag^+ concentration.

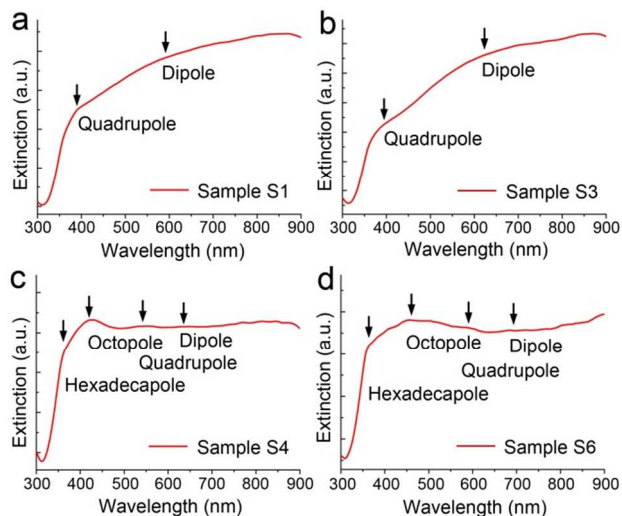


Fig. 6 UV-Vis spectra of Ag mesoparticles with different shapes, (a) S1: meatball-like, (b) S3: coral-like, (c) S4: urchin-like, and (d) S6: highly-branched morphologies.

the mesoparticle that induces overgrowth of the Ag mesoparticles. Similar with dopa molecules, the L-AA molecules also will promote the tips of mesoparticles to preferentially overgrowth, thus resulting in hierarchical morphology.

Usually, chemical reaction rate is increased by the increase of reactant agent concentration. At high concentration of Ag^+ ions, the reaction rate is quicker than that at medium and low concentrations. More Ag atoms will be produced in the first and second stages (Fig. 5b). The higher supersaturation concentration of Ag atoms induces more and smaller nanoparticles in the second stage. These nanoparticles will aggregate to form spherical mesoparticle under “glue” function of L-AA. Because of the quick reaction at high concentration, most of Ag^+ ions will be reduced into Ag atoms in the first three stages. Thus, in the last stage, there are not enough remaining Ag^+ ions for the mesoparticle overgrowth. Finally, only meatball-like mesoparticles are obtained. At medium and low concentrations of Ag^+ ions, the reaction rate becomes slow. The lower supersaturation concentration of Ag atoms is formed in the first two stages, which induces the formation of larger nanoparticles with lower density (ρ) in the solution. Depending on equation (2), smaller mesoparticles can be formed in the third stage. At the same time, more Ag^+ ions are remained, which is abundant to support the overgrowth of the small protrusions. Thus, longer and sharper protrusions are formed in the fourth stage. Overall, with the concentration of Ag^+ ions decreasing from high to low, the morphology of mesoparticles transforms from meatball-like to coral-like, urchin-like, and even to highly-branched shapes.

Optical and SERS properties

The UV-Vis extinction spectra of Ag mesoparticles with different morphologies were measured and shown in Fig. 6. The monodispersity of the mesoparticles allows the experimental observation of well-defined higher-order multipole plasmon modes in addition to the dipole resonance. The localized surface plasmon resonance (LSPR) is determined by particle size and morphology.

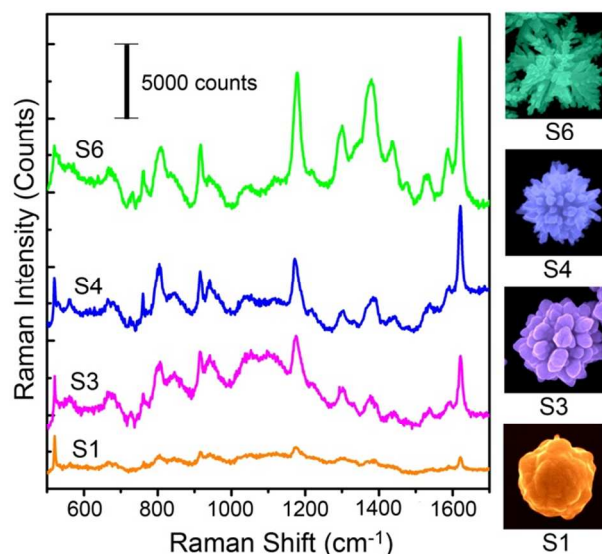


Fig. 7 Single-particle SERS properties of Ag mesoparticles with different topographies, S1: meatball-like, S3: coral-like, S4: urchin-like, and S6: highly-branched morphologies.

With the protrusions on the mesoparticle surface becoming longer and sharper, the UV-Vis spectra peaks corresponding to higher-order multipole plasmon resonance modes in addition to the dipole resonance, such as quadrupole, octupole and hexadecapole, become clear and can be observed. For the meatball-like and coral-like mesoparticles (sample S1 and S3 in Fig. 6a and b), only one higher-order multipole, i.e. quadrupole, extinction peak can be found. For the urchin-like and highly-branched mesoparticles (sample S4 and S6 in Fig. 6c and d), two more higher-order multipole, i.e. octupole and hexadecapole, is appeared.

The SERS properties of Ag mesoparticles with tunable morphologies were evaluated by using crystal violet (CV), a well-known and commonly used SERS analytes. The SERS spectra of CV molecules adsorbed on individual Ag mesoparticles with four typical morphologies, sample S1, S3, S4, and S6 (as shown in Fig. 1), were measured on a confocal microprobe Raman spectrometer under 633 nm excitation wavelength as Fig. S2 shown. Due to the excitation with 633 nm laser line lies in the absorption band of CV molecules resonance, at this situation, the obtained Raman signal belongs to the surface-enhanced resonance Raman scattering (SERRS). A fluorescent baseline will be formed in Raman spectra when CV molecules excited under 633 nm laser as shown in Fig. S4. The obtained SERRS spectra in Fig. 7 reveal the characteristic peaks of CV, for instance, at 1172, 1371, 1619 cm^{-1} , and correspond well to the ordinary Raman spectra of CV in the solid state and in aqueous solution.⁴⁴⁻⁴⁵ An apparent trend of increasing SERRS signal with increase of surface texture can be found: the signal intensities at 1172 cm^{-1} peak are found to scale as 1:5.1:6.2:13.9 for the mesoparticles S1, S3, S4, and S6, respectively. Following the procedure and assumptions described in previous report (details show in Supporting Information),³¹ the EFs of SERS for CV molecules on mesoparticles S1, S3, S4, and S6, are estimated to be about 5.0×10^6 , 1.3×10^7 , 1.8×10^7 , and 8.2×10^7 , respectively. These results are consistent with previous reports, such as the estimated

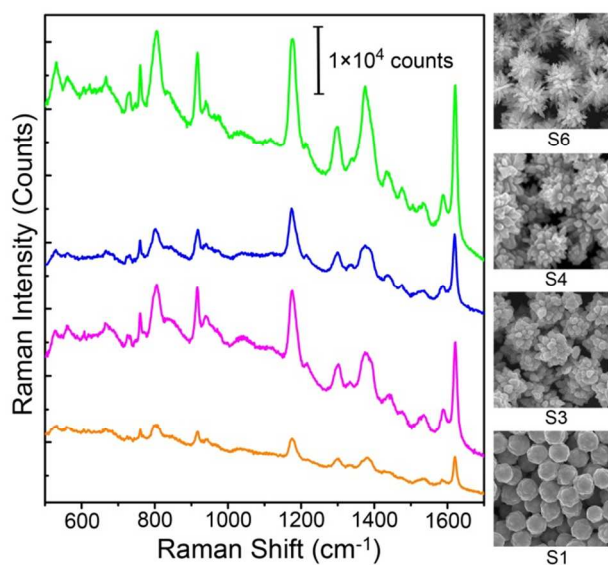


Fig. 8 SERRS properties from Ag mesoparticle aggregated films. The films are contributed by Ag mesoparticles with various shapes, S1: meatball-like, S3: coral-like, S4: urchin-like, and S6: highly-branched morphologies.

value of EFs $\sim 10^6$ - 10^7 for Au meatball-like mesoparticle and $\sim 10^7$ for Au urchin-like and Ag flower-like mesoparticles.^{9,29,33} In this study, EFs of the Ag meatball-like mesoparticle and urchin-like mesoparticle are 5.0×10^6 , and 1.8×10^7 , respectively.

Fig. 8 shows the SERRS spectra of CV molecules on particle aggregated films. Similar trend with the enhancement of single particle is found for the particle aggregated film. The EFs for sample S1, S3, S4, and S6 are about 4.4×10^8 , 8.7×10^8 , 6.9×10^8 , and 4.1×10^9 , respectively. In the measurement, the laser spot was 850 nm in diameter and the particle size was about 1 to 2 μm . So, as shown in Fig. S3, the detected area in the particle aggregated film was the border region between several particles. The aggregation of the hierarchical mesoparticles can greatly improve the enhancement of SERRS signal. This can be explained by the interparticle interactions in the particle aggregated film, which result in additional abundant

“hot spots”.⁴⁶ The Raman signal collection time was 20 s for single particle detection and 1 s for detection of particle aggregated film. Compared the signal intensity (1172 cm^{-1} peak) at Fig. 7 and 8, we can estimated that the enhancements of mesoparticle aggregated films are 88, 67, 38, and 50 times higher than that of single particle for sample S1, S3, S4, and S6, respectively. As reported in previous work, the EF for urchin-like Au mesoparticle film exceeded the EF of the corresponding individual particle by 10-100 times, which is consistent with our result.¹²

To corroborate the observed relationship between the SERS activity and surface topography of the hierarchical Ag mesoparticles, we applied the three-dimensional FDTD method to calculate the local electromagnetic field intensity around model particles irradiated with monochromatic light. Five model Ag mesoparticles were built and simulated using FDTD method. They had different surface topographies, model A: spherical particle with smooth surface, model B: meatball-like particle used to simulate the sample S1, model C: coral-like particle used to simulate the sample S3, model D: urchin-like particle used to simulate the sample S4, and model E: highly-branched particle used to simulate the sample S6. Their geometric parameters are shown in Supporting Information.

Fig. 9a-k show the typical distributions of the electric field E (plotted as color-code $|E|^2$) calculated in a plane across a vertical axis of these model particles irradiated from top by 633 nm light. It is generally agreed that the Raman intensity increases by a factor $|E|^4$ with respect to the local electric field on the SERS substrate surface.⁴⁷ The most localized and enhanced electromagnetic field areas (compared with the scale bars of color code in Fig. 9) are found in vicinity of tips and gaps on the highly nanotextured mesoparticle surface. Comparing the electromagnetic field distribution maps for model A and B (Fig. 9a-d), it can be found that the localized-electromagnetic field is excited by the nanoprotusions on the surface, as they act like nanolightning rods.³³⁻³⁴ From the comparison of the enhanced localized-electromagnetic field in the vicinity of nanoprotusions of model B, C and D (Fig. 9c-h), we can find that the longer and sharper protrusions on the surface can excite stronger electromagnetic field on their tip surfaces (as indicated by

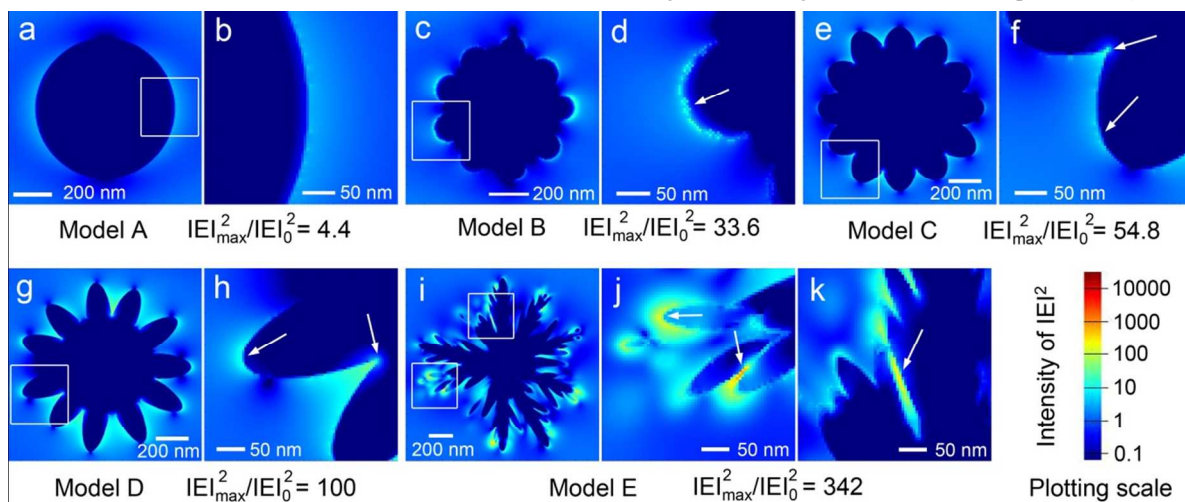


Fig. 9 The FDTD calculated electromagnetic field distribution and intensity of the individual Ag mesoparticles with various topographies under 633 nm incident laser, (a,b) model A: spherical mesoparticle, (c,d) model B: meatball-like mesoparticle, (e,f) model C: coral-like mesoparticle, (g,h) model D: urchin-like mesoparticle, and (i-k) model E: highly-branched mesoparticle. (b,d,f,h,j,k) Zoomed images from circled area.

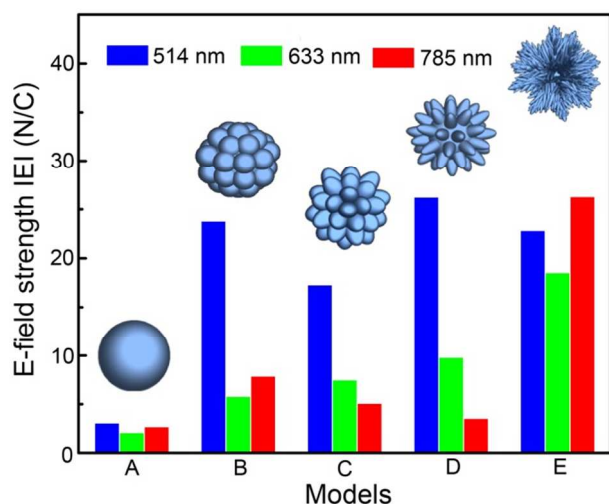


Fig. 10 Histograms of maximal electromagnetic field enhancements calculated from models A–E under excitation wavelengths of 514, 633, and 785 nm at x–y plane using FDTD calculation method.

arrows in Fig. 9d, f and h). Fig. 9f and h (as indication of arrows) reveal that enhanced localized-electromagnetic field also is excited in the gap formed between two protrusions. This can be explained as the exciting light will be confined in the cavity of gaps induced stronger surface plasmon resonance (SPR). Deeper and narrower gaps can more effectively confine the light in their cavity, resulting in stronger localized-electromagnetic field. Compared with coral-like and urchin-like mesoparticles, the highly branched mesoparticle has the sharpest protrusions and narrowest gaps on their surface. At the same time, the densities of protrusions and gaps are highest on the highly branched mesoparticle surface. Correspondingly, the number and intensity of SERS “hot spots” are largest on highly branched mesoparticle surface, as shown in Fig. 9i–k. So, the highly branched nanotextured topographies is clearly favored as the one potentially demonstrating the largest SERS enhancement (proportional to $\sim|E|^4$), in agreement with the experimental data.

Additionally, our FDTD simulation reveals that the excitation light wavelength also has effect on the intensity of localized-electromagnetic field. Fig. 10 displays the histograms of maximal electromagnetic field intensity calculated from models A–E at excitation wavelengths of 532, 633, and 785 nm in x–y plane. This result indicates that the effect of the excitation wavelength on the electromagnetic field is highly dependent on the textured topographies of the mesoparticles. If the excitation light wavelength matches the SPR of the metal nanostructure, stronger localized-electromagnetic field will be excited in the vicinity of nanoprotuberances and nanogaps. Compared to the model A to D, the highly branched Ag mesoparticles have an inhomogeneous surface texture and therefore likely exhibit broadened SPRs. Taking this into account, our FDTD simulations indicate that the optimal SERS excitation wavelength for highly branched mesoparticles would lie in the red and near-infrared spectral region, such as 633 and 785 nm, as shown in Fig. 10.

The extreme limit of single-particle SERS versus analyte concentration was evaluated on the highly-branched Ag

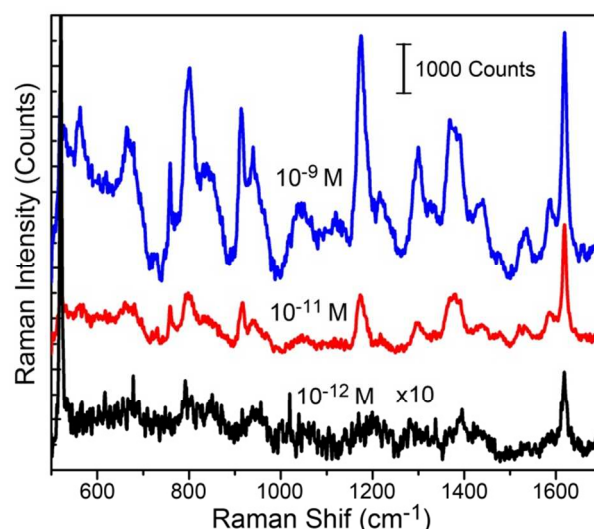


Fig. 11 Single-particle SERS spectra of CV molecules adsorbed on separated individual highly-branched Ag mesoparticles at decreased CV concentrations from 10^{-9} M to 10^{-11} M and 10^{-12} M.

mesoparticles. Quite diluted CV aqueous solution with concentrations from 1.0×10^{-9} to 1.0×10^{-12} M was used by depositing on the Ag mesoparticles substrate. As shown in Fig. 11, when the CV concentration decreases to 1.0×10^{-11} M, the spectral features close to the characteristic vibrational peaks of CV (1172 , 1371 , 1619 cm^{-1}) can still be easily identified. When the CV concentration decreases even to 1.0×10^{-12} M, some feature peaks (such as 1371 and 1619 cm^{-1}) still can be identified. Compared with previous study that the concentration extreme limit for Ag mesoparticles with rough surface were 1.0×10^{-11} and 1.0×10^{-12} M using CV solution.^{23,48} So, in this study, the single-particle highly-branched Ag mesoparticle also shows outstanding properties for the concentration extreme limit.

Conclusions

In summary, hierarchical Ag mesoparticles with various surface morphologies have been synthesized in a simple and green synthesis system. In this reaction system, AgNO_3 is only reduced by L-AA at room temperature without the addition of any other capping agents and organics. The surface topographies of the mesoparticle can be well tuned by changing the concentrations of AgNO_3 and L-AA. In this particle-mediated growth system, lower concentration will promote the anisotropic growth to form denser and sharper protrusions on the mesoparticle surface, which can greatly increase the SERS enhancement. The SERS EF of the arrayed highly branched Ag mesoparticles reaches to more than 10^9 . The FDTD simulation revealed that dense “hot spots” with the highest electromagnetic field was formed at the vicinity of tips and gaps between protrusions by the excited SPR under the irradiation of monochromatic light. This study will help to understand the relationship between topography and SERS properties.

Acknowledgements

This work was supported by National Natural Science Foundation of China (Nos. 51171139, 51201122, and 51202180), Natural Science Foundation of Shaanxi Province (No. 2012JQ6006), Doctoral Fund for New Teachers (Nos. 20120201120049 and 20110201120039) and the Fundamental Research Funds for the Central Universities (No. 08142008, 08142023 and 08143077). J. X. Fang was supported by Tengfei Talent Project of Xi'an Jiaotong University, the New Century Excellent Talents in University (NCET), and Scientific New Star Program in Shaanxi Province (No. 2012KJXX-03). G. Yang would thank Scientific Research Foundation for the Returned Overseas Chinese Scholars, State Education Ministry. The TEM work was done at International Center for Dielectric Research (ICDR), Xi'an Jiaotong University.

Notes and references

^a State Key Laboratory for Mechanical Behavior of Materials, School of Science, Xi'an Jiaotong University, Shaanxi, 710049, P. R. China. Email: hjyou@mail.xjtu.edu.cn; jxfang@mail.xjtu.edu.cn

^b Key Laboratory of the Ministry of Education and International Center for Dielectric Research, Xi'an Jiaotong University, Shaanxi, 710049, P. R. China

Electronic Supplementary Information (ESI) available: EDX analysis and calculation of SERS EFs. See DOI: 10.1039/b000000x/

- A. Campion, P. Kambhampati, *Chem. Soc. Rev.* 1998, **27**, 241.
- S. E. J. Bell, N. M. S. Sirimuthu, *Chem. Soc. Rev.* 2008, **37**, 1012.
- J. F. Li, Y. F. Huang, Y. Ding, Z. L. Yang, S. B. Li, X. S. Zhou, F. R. Fan, W. Zhang, Z. Y. Zhou, D. Y. Wu, B. Ren, Z. L. Wang, Z. Q. Tian, *Nature* 2010, **464**, 392.
- S. D. Hudson, G. Chumanov, *Anal. Bioanal. Chem.* 2009, **394**, 679.
- X. M. Wu, C. Xu, R. A. Tripp, Y. W. Huang, Y. P. Zhao, *Analyst* 2013, **138**, 3005.
- D. P. Cowcher, Y. Xu, R. Goodacre, *Anal. Chem.* 2013, **85**, 3297.
- Y. H. Zhao, W. Q. Luo, P. Kanda, H. W. Cheng, Y. Y. Chen, S. P. Wang, S. Y. Huan, *Talanta* 2013, **113**, 7.
- S. Gajaraj, C. Fan, M. S. Lin, Z. Q. Hu, *Environ. Monit. Assess.* 2013, **185**, 5673.
- H. Wang, N. J. Halas, *Adv. Mater.* 2008, **20**, 820.
- C. F. Tian, C. H. Ding, S. Y. Liu, S. C. Yang, X. P. Song, B. J. Ding, Z. Y. Li, J. X. Fang, *ACS Nano* 2011, **5**, 9442.
- M. F. Zhang, A. W. Zhao, H. H. Sun, H. Y. Guo, D. P. Wang, D. Li, Z. B. Gan, W. Y. Tao, *J. Mater. Chem.* 2011, **21**, 18817.
- J. X. Fang, S. Y. Du, S. Lebedkin, Z. Y. Li, R. Kruk, M. Kappes, H. Hahn, *Nano Lett.* 2010, **10**, 5006.
- Fleischm. M, P. J. Hendra, McQuilla. Aj, *Chem. Phys. Lett.* 1974, **26**, 163.
- M. Moskovits, *Rev. Mod. Phys.* 1985, **57**, 783.
- J. Bellessa, C. Symonds, K. Vynck, A. Lemaitre, A. Brioude, L. Beaur, J. C. Plenet, P. Viste, D. Felbacq, E. Cambril, P. Valvin, *Phys. Rev. B* 2009, **80**, 033303.
- W. Wu, G. Y. Jung, D. L. Olynick, J. Straznicky, Z. Li, X. Li, D. A. A. Ohlberg, Y. Chen, S. Y. Wang, J. A. Liddle, W. M. Tong, R. S. Williams, *Appl. Phys. A-Mater. Sci. Process.* 2005, **80**, 1173.
- Y. J. Chun, S. Nakajima, M. Kawabe, *Jpn. J. Appl. Phys. Part 2 - Lett.* 1996, **35**, L1075.
- S. Sakamoto, L. Philippe, M. Bechelany, J. Michler, H. Asoh, S. Ono, *Nanotechnology* 2008, **19**, 405304.
- X. Wen, G. Li, J. Zhang, Q. Zhang, B. Peng, L. M. Wong, S. Wang, Q. Xiong, *Nanoscale* 2014, **6**, 132.
- C. Cao, J. Zhang, X. Wen, S. L. Dodson, N. T. Dao, L. M. Wong, S. Wang, S. Li, A. T. Phan, Q. Xiong, *ACS Nano* 2013, **7**, 7583.
- S. Dodson, M. Haggui, R. Bachelot, J. Plain, S. Li, Q. Xiong, *J. Phys. Chem. Lett.* 2013, **4**, 496.
- J. M. Nam, D. K. Lim, K. S. Jeon, J. H. Hwang, H. Kim, S. Kwon, Y. D. Suh, *Nat. Nanotechnol.* 2011, **6**, 452.
- Z. Yang, L. Zhang, H. You, Z. Li, J. Fang, *Part. Part. Syst. Charact.* 2013, DOI: 10.1002/ppsc.201300290.
- B. Peng, G. Li, D. Li, S. Dodson, Q. Zhang, J. Zhang, Y. H. Lee, H. V. Demir, X. Yi Ling, Q. Xiong, *ACS Nano* 2013, **7**, 5993.
- X. M. Qian, X. H. Peng, D. O. Ansari, Q. Yin-Goen, G. Z. Chen, D. M. Shin, L. Yang, A. N. Young, M. D. Wang, S. M. Nie, *Nat. Biotechnol.* 2008, **26**, 83.
- L. Rodriguez-Lorenzo, R. n. A. Álvarez-Puebla, I. Pastoriza-Santos, S. Mazzucco, O. Stéphan, M. Kociak, L. M. Liz-Marzán, F. J. García de Abajo, *J. Am. Chem. Soc.* 2009, **131**, 4616.
- E. Nalbant Esenturk, A. R. Hight Walker, *J. Raman Spectrosc.* 2009, **40**, 86.
- H. X. Xu, E. J. Bjerneld, M. Kall, L. Borjesson, *Phys. Rev. Lett.* 1999, **83**, 4357.
- H. J. You, Y. T. Ji, L. Wang, S. C. Yang, Z. M. Yang, J. X. Fang, X. P. Song, B. J. Ding, *J. Mater. Chem.* 2012, **22**, 1998.
- M. J. Mulvihill, X. Y. Ling, J. Henzie, P. D. Yang, *J. Am. Chem. Soc.* 2010, **132**, 268.
- Z. Liu, F. Zhang, Z. Yang, H. You, C. Tian, Z. Li, J. Fang, *J. Mater. Chem. C* 2013, **1**, 5567.
- Y. Wang, P. H. C. Camargo, S. E. Skrabalak, H. Gu, Y. Xia, *Langmuir* 2008, **24**, 12042.
- H. Y. Liang, Z. P. Li, W. Z. Wang, Y. S. Wu, H. X. Xu, *Adv. Mater.* 2009, **21**, 4614.
- L. M. Tong, Z. P. Li, T. Zhu, H. X. Xu, Z. F. Liu, *J. Phys. Chem. C* 2008, **112**, 7119.
- F. Hao, C. L. Nehl, J. H. Hafner, P. Nordlander, *Nano Lett.* 2007, **7**, 729.
- H. You, C. Ding, X. Song, B. Ding, J. Fang, *CrystEngComm* 2011, **13**, 4491.
- J. P. Xie, Q. B. Zhang, J. Y. Lee, D. I. C. Wang, *ACS Nano* 2008, **2**, 2473.
- H. You, S. Yang, B. Ding, H. Yang, *Chem. Soc. Rev.* 2013, **42**, 2880.
- K. P. Velikov, G. E. Zegers, A. van Blaaderen, *Langmuir* 2003, **19**, 1384.
- L. Lu, A. Kobayashi, K. Tawa, Y. Ozaki, *Chemistry of Materials* 2006, **18**, 4894.
- Z. M. Peng, H. J. You, H. Yang, *ACS Nano* 2010, **4**, 1501.
- J. Fang, B. Ding, H. Gleiter, *Chem. Soc. Rev.* 2011, **40**, 5347.
- J. X. Fang, H. J. You, P. Kong, Y. Yi, X. P. Song, B. J. Ding, *Cryst. Growth Des.* 2007, **7**, 864.
- X. M. Qian, S. M. Nie, *Chem. Soc. Rev.* 2008, **37**, 912.
- K. Kneipp, Y. Wang, H. Kneipp, L. T. Perelman, I. Itzkan, R. Dasari, M. S. Feld, *Phys. Rev. Lett.* 1997, **78**, 1667.
- J. P. Xie, J. Y. Lee, D. I. C. Wang, *Chemistry of Materials* 2007, **19**, 2823.
- P. Dawson, J. A. Duenas, M. G. Boyle, M. D. Doherty, S. E. J. Bell, A. M. Kern, O. J. F. Martin, A. S. Teh, K. B. K. Teo, W. I. Milne, *Nano Lett.* 2011, **11**, 365.
- J. X. Fang, S. Y. Liu, Z. Y. Li, *Biomaterials* 2011, **32**, 4877.